Journal of Physics D:
Applied Physics

PAPER • **OPEN ACCESS**

Structure and phase dynamics in electrospray deposited amorphous MoO_3 via thermal treatment

To cite this article: M Azizinia *et al* 2025 *J. Phys. D: Appl. Phys.* **58** 125304

OPEN ACCESS
IOP Publishing
Journal of Physics D: Applied Physics
J. Phys. D: Appl. Phys. **58** (2025) 125304 (10pp)
https://doi.org/10.1088/1361-6463/ada9fc

Structure and phase dynamics in electrospray deposited amorphous MoO_3 via thermal treatment

M Azizinia[1], M Minicucci[1], R Gunnella[1,*], M Passacantando[2] and S J Rezvani[1,*]

[1] Sezione di Fisica, Scuola di scienze e tecnologie, Universitá di Camerino, Camerino 62032, Italy
[2] Department of Physical and Chemical Science, University of L'Aquila, Via Vetoio, 67100 Coppito, L'Aquila, Italy

E-mail: roberto.gunnella@unicam.it and sj.rezvani@unicam.it

Received 8 July 2024, revised 11 December 2024
Accepted for publication 14 January 2025
Published 29 January 2025

Abstract

Molybdenum oxides with distinct structures and phases have shown unique properties that are of interest in many scientific and technological applications. However, the scalability to large area deposition and in particular the deposition of surfaces with specific topology, with a uniform and controlled structure still remains a challenge. In this work, a uniform MoO_3 film with amorphous structure was achieved via electrospray deposition from fine particle dispersion in water. A high vapor pressure solvent was utilized for the progress of the deposition. As-deposited films with large thicknesses (<1 μm) show amorphous structures with a mean roughness lower than $\sim$32 nm. The deposited film was subsequently subject to thermal treatment with optimal thermodynamic parameters in order to modify the structure, the phase, the defect density and subsequently the electronic properties of the final structure. It is shown that a uniform coating layer with controlled structure and defect density can be achieved. This method facilitates the deposition of oxide layers on a variety of unconventional surfaces with large area as well as curved geometry.

Supplementary material for this article is available online

Keywords: structures, phases, dynamics, electrospray, amorphous, MoO3

1. Introduction

Transition metal oxides (TMOs), exhibiting elevated work functions and favorable opto-electronic characteristics have attracted considerable attention due to their promising potential in advanced applications such as photonics, thermochromic materials and protective coatings [1–6]. Among TMOs, molybdenum oxides in particular have been subject to extensive investigations due to their interplay between lattice configurations and multiple valence states of molybdenum [7, 8]. For instance, molybdenum trioxide (MoO_3) is a high dielectric constant insulator (high-k), while its electronic structure can be precisely tailored by adjusting oxygen sub-stoichiometry (MoO_{3-x}, where $0 < x < 1$), thereby introducing electronic states in the gap that significantly impact the oxides' electrical properties. In its stoichiometric form, MoO_3 exhibits n-type doped semiconducting characteristics. However, there is often an equilibrium concentration of

* Authors to whom any correspondence should be addressed.

defects, primarily oxygen vacancies, resulting in the creation of gap states. These n-type dopants result in a further adjustment of the MoO_3 Fermi level toward the conduction band [9–12]. A continuous reduction of oxygen content may further transform MoO_3 into MoO_2. MoO_2 is a low valence state of molybdenum that is stable, having Mo^{4+} cations with partially filled 4*d* band that results in a semi-metallic state [13].

Several attempts have been carried out for the deposition of MoO_3 with pre-designed properties, namely chemical vapor deposition [14], thermal evaporation [15], sol–gel process and ion-beam deposition method [16]. However, the methods mentioned above limit their application in fabrication of large-area devices with specific electronic properties. Moreover, most synthesis methods used in research laboratories are not economically feasible for industrial applications. The electrospray deposition method, on the other hand, offers numerous advantages in the synthesis and deposition of nanostructures due to the high precision control over droplet size and distribution. The electrospray deposition method allows uniform deposition of mesoscopic thin films with relatively large thicknesses. The use of diluted solutions in this method facilitates the deposition of materials with limited solubility, being extremely crucial for their scalability. The process also allows coating of high surface area and particular geometries such as curved surfaces. Electrospray can be used for both organic [17, 18] and inorganic compounds [19] as well as simultaneous multiple deposition which can facilitate the formation of multi-layer and hybrid structures. Moreover, its scalability, low-temperature processing, and lack of high vacuum requirements make it economically feasible.

Several attempts have been made to deposit TMOs using the electrospray method. Back *et al* [20] deposited vanadium suboxide (VO_x) functional inter-layers. They investigated several solvents such as methanol, isopropyl alcohol, n-butanol, and n-pentanol, to optimize the uniformity of the fabricated VO_x film. Chaturvedi *et al* [21] used electrospray deposition for zinc oxide (ZnO) films both with and without an electric field. Their solution consisted of zinc acetate dihydrate and ammonium acetate dissolved in methanol. ZnO films deposited with an electric field displayed more homogeneous and granular structures compared to those deposited without an electric field. Several studies have also been done on the electrospray fabrication of nanocomposites of aluminum/MoO_3 nanostripes [22] and aluminum/MoO_3 nanoparticles [23] using nitrocellulose and poly(vinylidene fluoride) as binders, respectively. Both studies employed a syringe pump with a flow rate of 4.0 $ml{\cdot}h^{-1}$ and applied high voltages (20 kV for the former and 13.5 kV for the latter) to successfully fabricate nanocomposites using electrospray. However, the use of chemical binders and high voltages are notable disadvantages of the fabrication method in this case. Suzuki *et al* [19] has conducted the only research on the electrospray deposition of MoO_3 nanofilms using an aqueous, chemical-free solution. Their study demonstrated the successful deposition of MoO_3 films via the electrospray technique and explored its potential application in organic photovoltaic cells. Although specific voltage magnitudes were not provided, they used additive solvents such as acetone, acetonitrile, N,N-dimethylformamide (DMF), and dimethyl sulfoxide (DMSO) to improve the surface morphology and uniformity of the MoO_3 thin film. The results indicate that acetone is the most suitable solvent for depositing the MoO_3 aqueous solution. However, the effects of deposition parameters, precise control over the material phase, and subsequent treatments on the deposited films require further investigation. Additionally, a comprehensive analysis of the structural and electronic properties of the fabricated films and strategies to tailor these properties remain unexplored.

In the present investigation, an electrospray method with optimized parameters using MoO_3 aqueous solution was employed with a subsequent thermal treatment in order to produce uniform MoO_3 films with a controlled phase and structure. The structural dynamics was investigated starting from an amorphous structure to a crystalline phase, using low annealing temperatures ($\leqslant$400 °C). The role of each parameter on the subsequent structural evolution and defect formation is investigated by various characterization methods and detailed analysis of the deposited films.

2. Experimental procedure

Electrospray deposition was performed using MoO_3 solution in deionized water (DI) with a nominal concentration of 0.05 wt% and a molarity of 3.45 mM. The solution of MoO_3 powder and DI water was kept under stirring for a period of 24 h. Acetone was added to the stirred solution afterward in an amount corresponding to approximately 30% of the total solution volume. The acetone can enhance the deposition rate due to its higher vapor pressure compared with the water. The higher vapor pressure of acetone can result in a higher droplet generation. The higher evaporation ratio prevents undesirable droplet spreading or coalescence and ensures the production of fine and evenly distributed particles that enhances the homogeneity of the fabricated films. Acetone can also reduce the surface tension of the solution as it fosters the formation of smaller and highly uniform droplets during electrospraying. This effect increases the precision and control in the nucleation process [19, 24, 25]. Finally, the resulting solution was filtered using a 0.45 μm pore size filter in order to eliminate possible residues or dispersed large particles.

The electrospray deposition setup is depicted in figure 1. The setup is entirely made of stainless-steel with a skimmer hole diameter of 2 mm. The exit slit has the same dimension as the skimmer hole diameter (2 mm). The sample is mounted on the holder using a mounting tongue. The chamber is a 4 cm diameter tube and maintained under atmospheric pressure. A pressure gradient is established between the low pressure created by the rotary pumps (down to 10^{-2} mbar) and the atmospheric pressure (ΔP). Regardless of the specific value of the

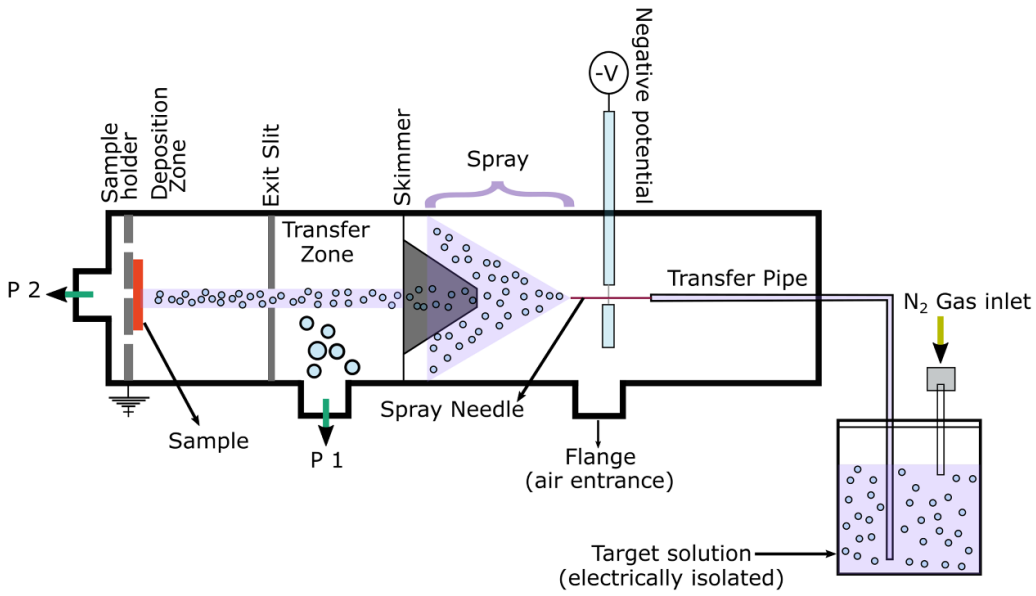

Figure 1. Schematic of the electrospray deposition apparatus employed for the MoO_3 deposition. The target solution is not connected to any electrical source and is injected into the chamber solely through precisely controlled nitrogen pressure. The solution passes through a needle connected to a negative potential.Then, the spray passes through the skimmers due to the pressure gradient created by pump P1, which removes large droplets after the explosion.The deposition chamber is under atmospheric pressure and the air is introduced into the chamber via an open flange. The pressure gradient is the difference between the minimum pressure of 10^{-2} mbar of the rotary pumps and the atmospheric pressure relative to the distance of the pump from the source needle. The small droplets afterwards pass through the exit slit via secondary gradient (P2) and are deposited on the grounded substrate.

ΔP which remains the same in all processes, the pressure is compensated via the N_2 pressure inserted into the solution. This is the pressure that results in the spray cone formation. In our case, it is considered that the rough pumps can achieve a few mTorr in the vacuum chamber and that the spray nozzle is at ambient pressure. Differential pumping guarantees only tens of Torr and is able to remove the larger neutral particles in the first section (in the transfer zone by ΔP1), while the hundreds of mTorr available for the P2 region (due to the pin-hole and skimmer separating transfer and deposition zones) can direct the residual smaller charged liquid particles to the sample. Lower N_2 pressure results in a large droplet formation and a higher pressure in a continuous flow of the solution. The ΔP1 helps in the evaporation of the larger droplets that are condensate majorly due to gravity, while the P2 guarantees a continuous flow toward the sample holder. In the absence of the P2, the particle will condensate on the chamber's wall due to the gravity and Coulomb force. The higher ΔP2 can increase the density of droplet deposition (e.g. using the TMP). The distance was chosen in a way to ensure that the uniform density of the particles arrive at the substrate ($\sim$40 cm from the hole of the skimmer) [17, 18]. The lower ΔP2 results in the wetting of the substrate and non-uniform deposition (see supporting information). The pressure gradients depend on the geometry of the deposition chamber, which can be tuned via the N_2 pressure. In our case, a constant solution flow rate was achieved by precise regulation of the N_2 gas inlet pressure, using a mass flow meter (MKS type 1259CC-05000SV) with the optimized N_2 inlet pressure set at 750 sccm (0.75 slm—see supporting information). The solution then transits through the stainless steel tip (inner diameter of 0.1 mm) with a negative potential of 2 kV to facilitate the Coulomb explosion process [26] while the substrate is kept grounded. The applied electric field at the spray needle causes the target aqueous solution to form a conical shape, known as a Taylor cone [27], and induces the emission of a thin jet from the cone's apex. This jet is then ejected from the tip of the Taylor cone and breaks up into charged microdroplets [26–29]. The voltage magnitude was set to 2 kV, depending on the specific design of the apparatus, mainly the distance from the tip to the skimmer (2 mm) and the pumping system (for more details see [17, 18, 30]).

Silicon wafers were chosen as substrates due to their widespread use in semiconductor and thin film deposition applications. The cleaning procedure of silicon wafers is relatively simple, ensuring a reproducible surface for the electrospray deposition process. It is also adapted for subsequent characterization techniques. Prior to the deposition, $\sim 1 \times 1$ cm^2 silicon wafers were cleaned via ultrasonic cleaner in acetone and ethanol and rinsed with DI water. The silicon wafers were then dipped in 10% HF solution in order to remove the native oxide and rinsed subsequently with DI water. The samples were deposited at room temperature for a 30 minute deposition period and subsequently underwent thermal treatment in air for 10 minute. Morphology of the samples was then examined using ZEISS Sigma 300 scanning electron microscopy (SEM), as well as atomic force microscopy (AFM) using a CSI Nano-Observer microscope in resonant mode. For AFM, an n-type Si cantilever was used, coated with Pt at a resonance frequency of $\sim$72 kHz with an elastic constant of 1–5 N m^{-1} (AppNano). Furthermore,

for detailed information about the atomic composition and the structure of the MoO_3 films, micro-Raman spectroscopy was performed using a green (λ = 532 nm) laser source and a Horiba iHR320 spectrometer equipped with a 1800 line/mm grating. The surface chemistry of the deposited film was also investigated via X-ray Photoelectron Spectroscopy (XPS) using a non-monochromatic aluminium source (K_α = 1486.6 eV). The crystalline structure of the films was studied by x-ray diffraction measurements in grazing incidence configuration (GIXRD) at an incident angle of the x-ray beam, with respect to the sample surface, of 1° using a Siemens D5000 diffractometer, equipped with copper anode (K_α, λ = 1.5406 Å) and a Göbel mirror used to collimate the incident x-ray beam.

3. Results and discussions

The deposition parameters such as the nitrogen flow pressure and the solution concentration were optimised in order to achieve the most uniform and homogeneous films. Our results show the optimal pressure of nitrogen flow to be 750 sccm with a solution concentration of 0.05 wt% (see the supporting information). Paparoni *et al* [15] have investigated the structural dynamics of amorphous MoO_3 films synthesized by the physical vapor deposition (PVD) method by in-situ Raman spectroscopy during the annealing process. Their results indicate that the amorphous films show the initiation of the phase transitions at around 200 °C with formation of the crystalline MoO_3 at around 400 °C. Hence, in this work we chose these two strategic temperature points in order to investigate the phase transition in our samples.

X-ray diffraction signals were used to investigate the crystallinity and lattice parameters of the synthesized films. Shown in figure 2 are the GIXRD diffractograms for the different samples of MoO_3 films. For the as-deposited (AD) samples and those annealed at 250 °C (A250), no peaks are observable, confirming their completely amorphous nature. In the upcoming analysis, SEM will reveal large flakes with increased crystallinity in the sample annealed at 250 °C, which are widely dispersed on the surface. However, the overall diffraction of the thick films shows no trace of crystallinity in this sample, consistent with the Raman spectra of the predominantly amorphous areas.

The intermediate amorphous phase formation via thermal treatment was also observed by Camacho–López *et al* [31] in which they report progression from an initial amorphous state to an intermediate amorphous state before crystallization into the stable orthorhombic α-MoO_3 phase, emphasizing the complexity of the transformation process. In the case of samples annealed at 400 °C (A400) a crystalline structure is visible. The peaks are located at 2θ = 12.78°, 23.42°, 25.77°, 27.41°, 33.26°, 33.90°, 35.58° and 39° are attributed the (020), (110), (040), (021), (101), (111), (041) and (060) crystallographic planes, respectively, and are specified as orthorhombic MoO_3 of JCPDS-ICDD card number 05-0508 [32]. These peaks are

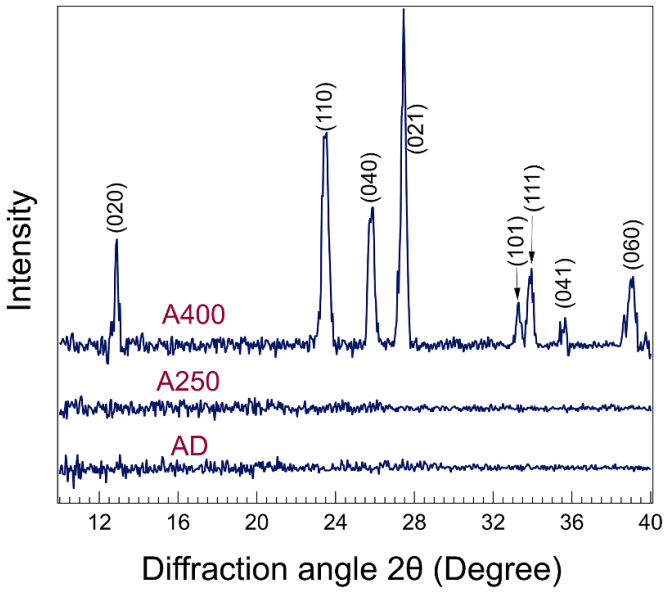

Figure 2. GIXRD patterns of MoO_3 as deposited film as well as after annealing at 250 °C and 400 °C in air.

in agreement with the XRD patterns reported for deposited α-MoO_3 films by microwave plasma [33] and hot wire-CVD [34] techniques.

The XRD results confirm that annealing at 400 °C causes the recrystallization of the amorphous MoO_3 and Mo suboxide into α-MoO_3 phase. This is a result of reoxidation in air during annealing and replenishment of the oxygen vacancies with available atmospheric oxygen, as reported previously [35]. Finally, the crystallite (D) size of the sample treated at 400 °C was estimated using the Scherrer equation $D = K\lambda/\beta\cos(\theta)$ where K is the Scherrer constant that most commonly is taken as 0.9 and characterizes the shape of the particle, λ is the wavelength (1.5406 Å), β is the full width of half maximum of the XRD peak, and θ is the Bragg angle. The D is calculated to be around 60 nm. This value is in excellent agreement with the small particles responsible for the signal broadening in the XRD spectrum. The large crystallites in the SEM image act like a bulk material while can affect the Raman signal to detect the enlargement by the signal ratio as discussed above.

The lattice spacing, $d_{(hkl)}$ and the lattice parameters (a, b, c) were estimated using Bragg's law, $d_{hkl} = n\lambda/2\sin\theta$, where ($hkl$) is the Miller indices of the plane being analysed, and n is the diffraction order. For the orthorhombic structure, d-spacing can also be written as $1/d^2_{(hkl)} = h^2/a^2 + k^2/b^2 + l^2/c^2$. The calculated lattice parameters are $a = 3.95$Å, $b = 13.84$Å, and $c = 3.68$Å which are also in good agreement with the reported values for the reference orthorhombic MoO_3 crystalline structure at the JCPDS-ICDD card number 05-0508 ($a = 3.96$Å, $b = 13.85$Å and $c = 3.69$Å) [32].

The morphology of the AD and after-thermal treatment MoO_3 films were investigated via SEM and illustrated in figure 3. The AD films show a disordered porous-like structure with aggregated particles forming a continuous film. After annealing at 250 °C the sample shows the formation of large

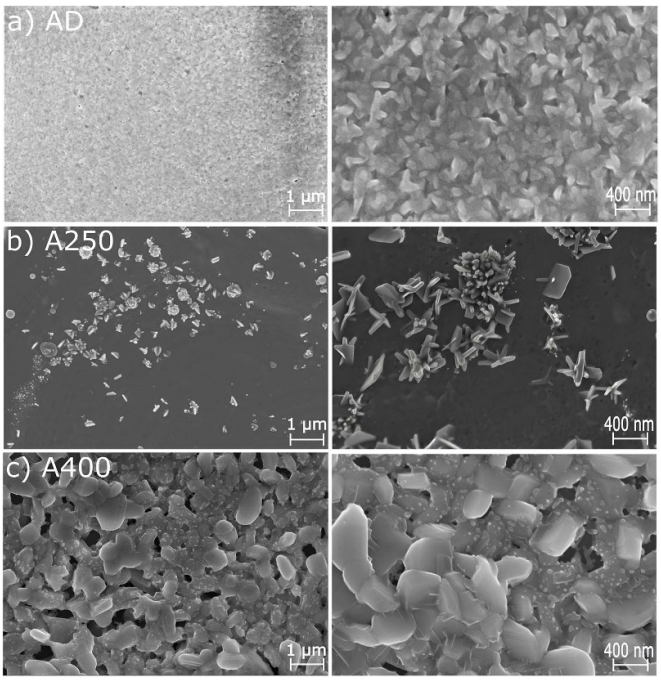

Figure 3. SEM images of (a) AD sample, along with the sample (b) A250, and (c) A400. The crystalline grains are clear in the sample thermally treated at 400 °C (c).

particles with a relative dimension of ∼200 nm with whisker-like shapes atop the continuous film. These structures likely arise from the Mo suboxide matrix, with a larger volumetric cell, leading to the formation of distinct islands. Further annealing at 400 °C demonstrates the nucleation and crystallization of the film into a granular structure with the grain dimension of ∼300–400 nm decorated with smaller particles of ∼30–50 nm. Energy-Dispersive X-ray Spectroscopy on all the samples shows the presence of Mo and O peaks as well as Si, with the exception of carbon, and does not evidence any further contamination (as shown in figure 4 in the supplementary information).

The detailed surface topography of the samples was investigated using atomic force microscopy. The AFM topography is in agreement with the observed morphology by SEM, indicating the formation of a smooth uniform AD film with a thickness and mean roughness of 1 μm and ∼ 9 nm, respectively (see figure 4). Microscopy on thermally treated samples at 250 °C was performed on areas without sharp whiskers to prevent instrumental damage. The samples also show a uniform film with a large particle formation on top increasing the mean roughness to ∼25 nm. On the other hand, the sample annealed at 400 °C, in agreement with the GIXRD results shows clear crystalline grains and a mean roughness of ∼32 nm.

Structural analysis of the samples was conducted via micro-Raman spectroscopy. Figure 5 presents the micro-Raman spectra of the AD sample and the annealed ones, as well as, the reference powder (used for the deposition). The spectrum of the AD sample exhibits broad features at 840–860 cm^{-1} and 950 cm^{-1}. These components can be assigned to amorphous MoO_3. The low frequency components at around 120, 136, 284 cm^{-1} are also assigned to amorphous MoO_3 [15, 31, 36]. The sample also shows components at about 180, 220, 370 and 440 cm^{-1} that can be attributed to MoO_2 and Mo_4O_{11} or reduced oxides, i.e. Mo_xO_{3x-1} [35, 37–40]. Features of the silicon substrate (with native oxide) are visible at 521 cm^{-1} (removed from all the spectra) and ∼965 cm^{-1}. The sample annealed at 250 °C (labeled as A250 in figure 5) exhibits features, similar to the as deposited sample indicative of a mixed complex structure, composed of both amorphous MoO_3 and reduced suboxide, e.g. Mo_4O_{11}, and MoO_2. However, while the micro Raman spectra measured on the wiskers show similar phase distribution, they demonstrate a higher level of crystallinity. It is evident that the sample exhibits structural variation with top layer whiskers containing crystalline structures, while the main sample structure remains predominantly amorphous. In general, while the A250 spectrum in red shows amorphous MoO_3 features, for the blue spectrum, the Raman peaks at 126, 150, 240, 284, 337, 374, 817 and 989 cm^{-1} display the typical vibrational features of the α-MoO_3 (see table 1). Despite the presence of this component at 816 cm^{-1}, a significant amorphous component is still present. Moreover, it is evident that the intensity of the peaks ranging from 168 to 240 cm^{-1} and around 370 cm^{-1} increases after annealing at 250 °C and a broad peak appears at 670 cm^{-1}, which was not present in the AD sample. These peaks are associated with mainly orthorhombic Mo_4O_{11} as well as MoO_2 [37, 39, 41]. The reduction of the MoO_3 to lower states has been reported in several previous investigations, particularly via annealing in vacuum conditions. The MoO_2 formation is also known to occur via an intermediate metastable phase, namely Mo_4O_{11}. These results suggest the initiation of oxygen configuration rearrangement in the defective structures at high temperatures, leading to partial reduction and metastable phase formation.

On the other hand, the sample annealed at 400 °C evidences sharp Raman components at 118, 129, 158, 198, 216, 246, 285, 292, 337, 364, 378, 470, 665, 816 and 992 cm^{-1} that are in good agreement with the peak positions of the reference MoO_3 powder (see table 1). This observation suggests the reoxidation and rearrangement of the matrix into a predominantly crystalline α-MoO_3 structure at this temperature.

It has been previously suggested that thermal treatment of MoO_3 in air can result in the formation of a defective crystal matrix, while annealing in vacuum results in the reduction of MoO_3 to MoO_2 [15, 42–44]. In the case of the present study, this phase transformation is closely related to the inherent oxygen reactivity of disordered MoO_3, which tends to lose interlayer oxygen easily during the annealing process. Specifically, in a rapid annealing process similar to our experiment, it is suggested that MoO_3 can readily interact with nitrogen and water vapor from the air, leading to the loss of interlayer oxygen in the initial stages. As a result, metastable phases such as MoO_{3-x} (with oxygen vacancies) or Mo_4O_{11} can form as will be discussed later. If this reduction persists for a short period, a stable MoO_2 phase may also emerge. However, at higher temperatures, the increased kinetic energy of diffusing oxygen atoms from the air can compensate for the oxygen

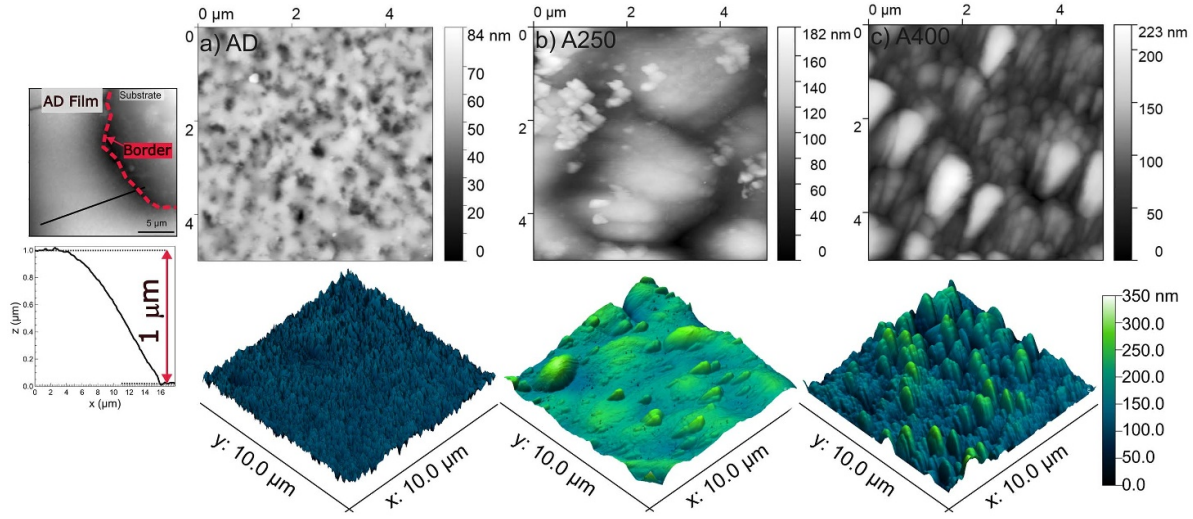

Figure 4. Left) AFM thickness profile measurement of the AD sample at the border of the film with the substrate, using a $20 \times 20\ \mu m^2$ AFM image. The dashed line shows the border between the film and the substrate and the profile is taken along the line indicated with the solid line. Right) AFM $5 \times 5\ \mu m^2$ images of MoO_3 samples deposited on Si substrates: (a) The AD sample reveals a spongy-like structure, uniformly distributed across the entire sample surface. (b) Upon annealing at 250 °C, the A250 sample exhibits formation of dispersed crystallites and (c) Following annealing at 400 °C, the sample undergoes crystallization.

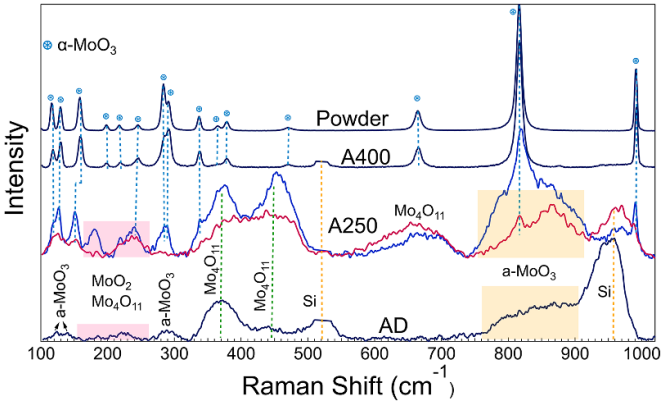

Figure 5. Raman spectra of amorphous MoO_3 (α- MoO_3) films as-deposited (AD), after annealing at 250 °C (A250), 400 °C (A400) and the bulk MoO_3 powder used for the deposition.

deficiencies, allowing the intermediate phases to reoxidize and stabilize back to the MoO_3 phase [35, 40, 45].

The defective structures resulting from the annealing process are usually evidenced via the presence of oxygen vacancies and distorted crystalline structures. The former condition results in the modification of the Mo/O intensity ratio of the $B_{2g}\sigma(O = Mo)$ and $B_{3g}\sigma(\mathrm{O} = \mathrm{Mo})$ modes and the latter condition leads to the shift in the B_{2g} and B_{3g} scattering features. The ratio of the components I_{284}/I_{292} is proposed to be a fingerprint of the stoichiometry of the MoO_3. Moreover, the ratio of the B_{2g} and B_{3g} modes (at 118 and 129 cm^{-1}, respectively), hereafter called I_{129}/I_{118}, is suggested to be correlated to the dimensions of crystalline grains [46, 47]. Our sample, annealed at 400 °C shows an inversion of the intensity of the peaks at 284 and 292 cm^{-1} ($B_{2g}\sigma(\mathrm{O} = \mathrm{Mo})$ and $B_{3g}\sigma(\mathrm{O} = \mathrm{Mo})$ modes), in comparison with the powder reference, confirming the presence of the defective structure, primarily due to distortions on the *c*-axis induced by oxygen vacancies [46].

To quantify the oxygen concentration in our samples, the I_{284}/I_{292} Raman intensity ratios were used by application of a linear fit, based on the approach reported by Dieterle *et al* [46]. in bulk MoO_3 powder with different treatment conditions. In figure 6, the results of our analysis on the ratio of oxygen-to-molybdenum and the final stoichiometry of the samples (x in MoO_x) along with the MoO_3 powder are depicted. Our results (in red) are also compared with the observations of Dieterle *et al* [46], as well as, with the outcomes of Castro Silva *et al* [36], derived from the annealing of MoO_3 at 400 °C in an O_2 atmosphere. Furthermore, recent results on amorphous MoO_3 films deposited via PVD on silicon substrate and subjected to thermal treatment at 410°C under different air partial pressures are also depicted in the image. The x values in our samples were annealed at 250 °C and 400 °C, i.e. A250 and A400, have been determined to be $x = 2.945$ that deviates from the source powder ($x = 2.957$) indicating the presence of a larger defect density in the resulted film. When the sample is annealed at 250 °C since the splitting of the peaks is hampered, it is suggested that x is definitely lower than 2.94, having a larger density of defects, while the approximate x using the flake spectra of the sample A250 is calculated to be slightly higher value of $x \geqslant 2.942$.

Raman analysis shows that the partial dissolution of MoO_3 powder in DI water and the subsequent deposition using electrospray results in the formation of disordered films with high density defects/vacancies. However, thermal treatment in an oxygen rich environment can lead to the reoxidation of the vacancies, resulting in a more stoichiometric state through oxygen incorporation. This process speeds up via a

Table 1. Raman peaks obtained from the source powder, samples A400 and A250.

Powder	A400	A250	Assignments
116 cm^{-1}	118 cm^{-1}		B_{2g}
129 cm^{-1}	129 cm^{-1}	127 cm^{-1}	B_{3g}
158 cm^{-1}	158 cm^{-1}	150 cm^{-1}	A_g-$\sigma(O_2Mo_2)_n$
198 cm^{-1}	198 cm^{-1}		B_{2g}-τ(Mo = O)
217 cm^{-1}	216 cm^{-1}	217 cm^{-1}	A_g-$\sigma(OMo_2)$
245 cm^{-1}	246 cm^{-1}	240 cm^{-1}	B_{3g}-τ(Mo = O)
284 cm^{-1}	285 cm^{-1}		B_{2g}-σ(O = Mo)
292 cm^{-1}	292 cm^{-1}	288 cm^{-1}	B_{3g}-σ(O = Mo)
337 cm^{-1}	337 cm^{-1}	335 cm^{-1}	A_g-$\sigma(OMo_3)$
364 cm^{-1}	364 cm^{-1}		A_g-σ(O = Mo)
378 cm^{-1}	378 cm^{-1}	374 cm^{-1}	B_{1g}-σ(O = Mo)
470 cm^{-1}	470 cm^{-1}	457 cm^{-1}	B_{1g}-$\nu(OMo_3)$
665 cm^{-1}	665 cm^{-1}		B_{3g}-$\nu(OMo_3)$
816 cm^{-1}	816 cm^{-1}	818 cm^{-1}	B_{1g}-$\nu(OMo_2)$
992 cm^{-1}	992 cm^{-1}	990 cm^{-1}	B_{1g}-ν(O = Mo)

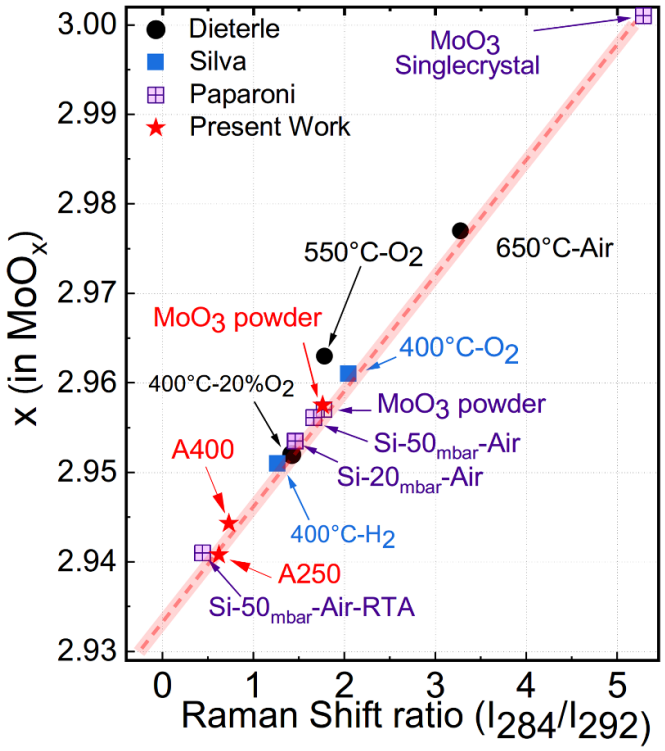

Figure 6. The stoichiometry of the samples is determined based on the intensity ratio of the $B_{2g}\sigma$(O = Mo) and $B_{3g}\sigma$(O = Mo) modes of MoO_3 at around 284 and 292 cm^{-1}, respectively. The value of x, has been computed using the linear trend equation reported by Dieterle *et al* [46]. Additionally, comparisons with the results of de Castro Silva *et al* [47] have been incorporated into the analysis. The results of Paparoni *et al* [15], after thermal treatment at 410°C in 20 mbar and 50 mbar air pressure, as well as rapid thermal annealing (20 °C min^{-1}) in 50 mbar air, labeled RTA.

temperature increase resulting in the formation of meta-stable suboxides (e.g. Mo_4O_{11}) at 250 and α-MoO_3 at 400 °C.

The phase structure and surface chemistry of the samples were also investigated via x-ray photoemission spectroscopy (see figure 7). The deconvolution of the Mo 3d $_{5/2}$ core level reveals three distinct components for all three samples at ∼233.2, ∼232.6, ∼231.5 eV attributed to the Mo^{6+}, Mo^{n+} ($4 < n < 6$) and Mo^{4+} corresponding to MoO_3, suboxide such as Mo_4O_{11} as well as the defective structure and MoO_2, respectively, with distinct relative intensities. At higher binding energy Mo $3d_{3/2}$ peaks with the same components as the Mo $3d_{5/2}$ peaks (with spin-orbit splitting equal to 3.15 eV) and small satellite lines are visible. The slight shift in the peak positions of similar compounds in different samples (see table 2) can be attributed to the presence of disordered phases and the absence of a well-defined crystal lattice [48].

The as deposited sample shows a higher concentration of Mo^{n+} signal (∼40% of the whole peak area) that corresponds

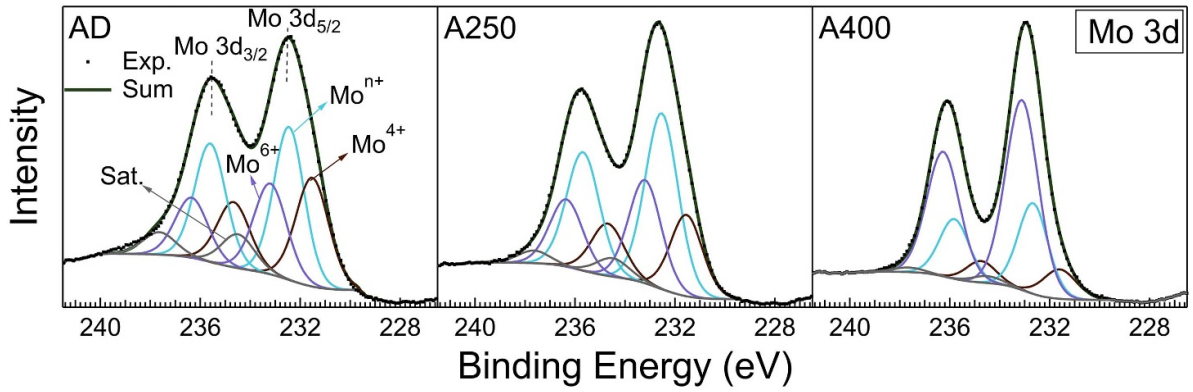

Figure 7. Mo 3d spectra of the AD sample, as well as the samples annealed at 250 °C and 400 °C along with the corresponding fits.

Table 2. Parameters used for peak-fitting of the Mo $3d_{5/2}$ peaks of the samples. The spin-orbit splitting between $3d_{3/2}$ and $3d_{5/2}$ states is approximately 3.2 eV.

	Peak position (eV)		
Valence state	AD	A250	A400
Mo^{6+}	233.20	233.20	233.15
Mo^{n+}	232.45	232.55	232.65
Mo^{4+}	231.5	231.55	231.6
Satellite	234.5	234.5	234.5

to the formation of the defective structures and/or suboxide. On the other hand, this sample shows a lower concentration of Mo^{4+} (28%) and Mo^{6+} (23%). The sample, annealed at 250 °C, shows an increase in the concentration of Mo^{6+} (27% of peak area) while the Mo^{n+} component intensity increases to 49% as well. The Mo^{4+} relative intensity decreases to 21%. In samples annealed at 400 °C, the Mo^{6+} (62%) phase is dominant although the suboxide and Mo^{4+} phases are still present at lower intensities (27% and 9%, respectively).

These results are in agreement with Raman spectroscopy, indicating a disordered structure in the AD film which transforms into meta-stable phases (e.g. Mo_4O_{11} and MoO_2) by thermal treatment at intermediate temperatures (250 °C) due to the loss of interlayer oxygen in the MoO_3 structure. This is confirmed via an increase in the Mo^{5+} components observed in the XPS spectra. Finally, thermal treatment at 400 °C triggers the reoxidation of the films into the MoO_3 crystalline phase (indicated by a relative increase in the Mo^{6+} in the XPS spectra). These results are also in good agreement with the results of Diskus *et al.,* describing the annealing-induced transformation of MoO_3 films into polycrystalline α-MoO_3 [49]. However, they have reported a crystallization pathway that involves significant mass transport and the formation of meta-stable β-MoO_3 before transforming into the orthorhombic α-MoO_3 phase. In the present study, no trace of β-MoO_3 was observed during the phase transition, neither by Raman spectroscopy nor by x-ray diffraction (see figure 2). The β-phase formation is believed, however, to be dependent on the treatment velocity and the rate that has a significant role in the formation of the β-phase. Upon annealing at 250 °C, we have observed the formation of Mo_4O_{11}, which is in agreement with numerous previous results identifying Mo_4O_{11} as an intermediate product during the MoO_3 reduction or the reoxidation of MoO_2 to MoO_3. Dang *et al* [50] report formation of Mo_4O_{11} as the intermediate phase, while hydrogen reduction from MoO_3 to MoO_2 at high temperatures. Similarly, Lalik [51] proposes a reduction mechanism of well crystalline MoO_3 at 550 °C with hydrogen gas, which confirms the formation of Mo_4O_{11} in oxygen transport from MoO_3 to MoO_2. In another study, Wang *et al* [52] investigates reduction of high-purity MoO_3 to MoO_2 using mixed CO and CO_2 gases at elevated temperatures and reported a three-step reduction process: $MoO_3 \rightarrow Mo_9O_{26} \rightarrow Mo_4O_{11} \rightarrow MoO_2$. These results suggest that crystallization and phase formation paths can be modulated by tuning the thermodynamic parameters of the thermal treatment procedure, which can result in distinct phase dynamics. However, the detailed thermodynamics of the nucleation and growth of the electrospray deposited MoO_3 still requires further investigation.

4. Conclusions

In the present work, the structural and electronic properties of the electrospray deposited amorphous molybdenum trioxide layers by the dissolution of the dispersed crystalline nanoparticles were investigated. The results show the formation of the amorphous/disordered layer at the initial stage with large density of defects. The defect density is a result of oxygen vacancy formation as well as metastable suboxide formation. It has been shown that the structure and defect density of the synthesized film can be tuned via further thermal treatments. The thermal treatment at low temperatures leads to the domination of metastable and intermediate suboxides (e.g. Mo_9O_{26} and Mo_4O_{11}) due to the reduction of the MoO_3 interlayer oxygen atoms. While at higher temperatures, the oxygen vacancies dominate the defect density in the highly crystalline α-MoO_3 lattice. The defect density is calculated to be ∼5%–6% which is in agreement with the previously reported results on films fabricated via PVD. This method facilitates the fabrication of scalable deposition of metal oxides with predesigned structure and relative defect density that can be exploited in

several applications at the industrial level. Further investigations on precise electronic configuration and electronic transport properties of the films are needed for establishment of the defect dynamics and improvements of the film characteristics.

Data availability statement

All data that support the findings of this study are included within the article (and any supplementary files).

Acknowledgment

This material is based upon work supported by the Air Force Office of Scientific Research under Award No. FA8655-20-1-7049 and Award No. FA8655-23-1-7004. We acknowledge the support of European Union—Next Generation EU MUR Project PE 0000023-NQSTI and Innovation Ecosystem Grant ECS 00000041 Vitality.

ORCID iDs

M Azizinia https://orcid.org/0000-0003-2483-5806
R Gunnella https://orcid.org/0000-0003-4739-6375
S J Rezvani https://orcid.org/0000-0002-6771-170X

References

[1] Tyagi A, Banerjee S, Cherusseri J and Kar K K 2020 Characteristics of transition metal oxides *Handbook of Nanocomposite Supercapacitor Materials I. Springer Series in Materials Science* vol 300, ed K Kar (Springer)
[2] Greiner M T, Chai L, Helander M G, Tang W-M and Lu Z-H 2012 Transition metal oxide work functions: the influence of cation oxidation state and oxygen vacancies *Adv. Funct. Mater.* **2** 4557–68
[3] Yu X, Marks T J and Facchetti A 2016 Metal oxides for optoelectronic applications *Nat. Mater.* **15** 383–96
[4] Diao F and Wang Y 2018 Transition metal oxide nanostructures: premeditated fabrication and applications in electronic and photonic devices *J. Mater. Sci.* **53** 4334–59
[5] Morales-Luna M, Tomás S, Arvizu M, Pérez-González M and Campos-Gonzalez E 2017 The evolution of the Mo^{5+} oxidation state in the thermochromic effect of MoO_3 thin films deposited by rf magnetron sputtering *J. Alloys Compd.* **722** 938–45
[6] Luo Q, Wang X, Yin K, Yu D and Lin H 2023 A method locating Cu-Ti-based glass formers using Ni-Zr binary clusters *J. Non-Cryst. Solids* **621** 122607
[7] Cong S *et al* 2017 Modifying the valence state of molybdenum in the efficient oxide buffer layer of organic solar cells via a mild hydrogen peroxide treatment *J. Mater. Chem.* **5** 889–95
[8] Hanson E D, Lajaunie L, Hao S, Myers B D, Shi F, Murthy A A, Wolverton C, Arenal R and Dravid V P 2017 Systematic study of oxygen vacancy tunable transport properties of few-layer MoO_{3-x} enabled by vapor-based synthesis *Adv. Funct. Mater.* **7** 1605380
[9] Khilla M, Hanafi Z, Farag B and Abu-el Saud A 1982 Transport properties of molybdenum trioxide and its suboxides *Thermochim. Acta* **54** 35–45
[10] Kashfi-Sadabad R, Yazdani S, Huan T D, Cai Z and Pettes M T 2018 Role of oxygen vacancy defects in the electrocatalytic activity of substoichiometric molybdenum oxide *J. Phys. Chem.* C **122** 18212–22
[11] Vasilopoulou M *et al* 2012 The influence of hydrogenation and oxygen vacancies on molybdenum oxides work function and gap states for application in organic optoelectronics *J. Am. Chem. Soc.* **134** 16178–87
[12] Zhang W, Li H, Firby C J, Al-Hussein M and Elezzabi A Y 2019 Oxygen-vacancy-tunable electrochemical properties of electrodeposited molybdenum oxide films *ACS Appl. Mater. Interfaces* **11** 20378–85
[13] Garland B M, Fairley N, Strandwitz N C, Thorpe R, Bargiela P and Baltrusaitis J 2022 A study of *insitu* reduction of MoO_3 to MoO_2 by x-ray photoelectron spectroscopy *Appl. Surf. Sci.* **598** 153827
[14] Abdellaoui A, Martin L and Donnadieu A 1988 Structure and optical properties of MoO_3 thin films prepared by chemical vapor deposition *Phys. Status Solidi* a **109** 455–62
[15] Paparoni F *et al* 2022 Metallic interface induced ionic redistribution within amorphous MoO_3 films *Adv. Mater. Interfaces* **9** 2200453
[16] Prasad A K, Kubinski D J and Gouma P-I 2003 Comparison of sol–gel and ion beam deposited MoO_3 thin film gas sensors for selective ammonia detection *Sensors Actuators* B **93** 25–30
[17] Abbas M, Ali M, Shah S K, D'Amico F, Postorino P, Mangialardo S, Guidi M C, Cricenti A and Gunnella R 2011 Control of structural, electronic and optical properties of eumelanin films by electrospray deposition *J. Phys. Chem.* B **115** 11199–207
[18] Ali M, Abbas M, Shah S K, Bontempi E, Colombi P, Di Cicco A and Gunnella R 2011 Variability of physical characteristics of electro-sprayed poly(3-hexylthiophene) thin films *J. Appl. Phys.* **110** 054515
[19] Suzuki K, Fukuda T, Liao Y and Bansal V 2014 Electrosprayed molybdenum trioxide aqueous solution and its application in organic photovoltaic cells *PLoS One* **9** e106012
[20] Back H, Kong J, Kang H, Kim J, Kim J-R and Lee K 2014 Flexible polymer solar cell modules with patterned vanadium suboxide layers deposited by an electro-spray printing method *Sol. Energy Mater. Sol. Cells* **130** 555–60
[21] Chaturvedi N, Swami S K, Kumar A and Dutta V 2014 Role of zno nanostructured layer spray deposited under an electric field in stability of inverted organic solar cells *Sol. Energy Mater. Sol. Cells* **126** 74–82
[22] Li Y, Ren H and Xie Q 2024 Electrospray nested energetic cells from nanothermite with MoO_3 nanostrips: Reactivity, sensitivity and combustion performance *Appl. Sci.* **14** 5522
[23] Chen J, Guo T, Yao M, Song J, Ding W, Mao Y, Li S and Zhu R 2020 Thermal behavior and combustion performance of al/MoO_3 nanothermites with addition of poly (vinylidene fluorine) using electrospraying *Mater. Res. Express* **7** 115009
[24] Jaworek A 2007 Electrospray droplet sources for thin film deposition *J. Mater. Sci.* **42** 266–97
[25] Gañan-Calvo A M 1994 20.O.05 the size and charge of droplets in the electrospraying of polar liquids in cone-jet mode and the minimum droplet size *J. Aerosol Sci.* **5** 309–10
[26] Gaskell S J 1997 Electrospray: principles and practice *J. Mass Spectrom.* **32** 677–88
[27] Taylor G I 1969 Electrically driven jets *Proc. R. Soc.* A **313** 453–75
[28] Rosell-Llompart J, Grifoll J and Loscertales I G 2018 Electrosprays in the cone-jet mode: from taylor cone formation to spray development *J. Aerosol Sci.* **125** 2–31
[29] Jeong J-h, Park K, Kim H, Park I, Choi J and Lee S S 2022 Multiplexed electrospraying of water in cone-jet mode

using a uv-embossed pyramidal micronozzle film *Microsyst. Nanoeng.* **8** 110
[30] Parmar R, de Freitas Neto D, Kazim S, Rezvani S, Rosolen J, Gunnella R, Amati M and Gregoratti L 2021 Manganese vanadium sulfate-oxide cylindrical core-shell heterostructures by electro-spray deposition on graphite foil for li^+ ion intercalation *J. Alloys Compd.* **888** 161483
[31] Camacho-López M, Haro-Poniatowski E, Lartundo-Rojas L, Livage J and Julien C 2006 Amorphous–crystalline transition studied in hydrated MoO_3 *Mater. Sci. Eng.* B **135** 88–94
[32] Diffract P 2001 File, JCPDS-ICDD, 12 campus boulevard, newtown square, PA 19073–3273
[33] Klinbumrung A, Thongtem T and Thongtem S 2012 Characterization of orthorhombic α-MoO_3 microplates produced by a microwave plasma process *J. Nanomater.* **012** 10–10
[34] Jadkar V, Pawbake A, Waykar R, Jadhavar A, Mayabadi A, Date A, Late D, Pathan H, Gosavi S and Jadkar S 2017 Synthesis of orthorhombic-molybdenum trioxide (α-MoO_3) thin films by hot wire-CVD and investigations of its humidity sensing properties *J. Mater. Sci., Mater. Electron.* **8** 15790–6
[35] Martín V C-S, Morales-Luna M, García-Tinoco P, Pérez-González M, Arvizu M, Crotte-Ledesma H, Ponce-Mosso M and Tomás S 2018 Chromogenic MoO_3 thin films: thermo-, photo- and electrochromic response to working pressure variation in rf reactive magnetron sputtering *J. Mater. Sci., Mater. Electron.* **29** 15486–95
[36] Sivakumar R, Gopalakrishnan R, Jayachandran M and Sanjeeviraja C 2007 Characterization on electron beam evaporated α-MoO_3 thin films by the influence of substrate temperature *Curr. Appl. Phys.* **7** 51–59
[37] Santagata A *et al* 2022 Enhanced and selective absorption of molybdenum nanostructured surfaces for concentrated solar energy applications *Materials* **15** 8333
[38] Wang H *et al* 2021 Nanostructured molybdenum-oxide anodes for lithium-ion batteries: an outstanding increase in capacity *Nanomaterials* **12** 13
[39] Borovšak M, Šutar P, Goreshnik E and Mihailovic D 2015 Topotactic changes on η-mo_4o_{11} caused by biased atomic force microscope tip and cw-laser *Appl. Surf. Sci.* **354** 256–9
[40] Lee S-H, Seong M J, Tracy C E, Mascarenhas A, Pitts J R and Deb S K 2002 Raman spectroscopic studies of electrochromic a-MoO_3 thin films *Solid State Ion.* **147** 129–33
[41] Dieterle M and Mestl G 2002 Raman spectroscopy of molybdenum oxides part II. Resonance raman spectroscopic characterization of the molybdenum oxides Mo_4O_{11} and MoO_2 *Phys. Chem. Chem. Phys.* **4** 822–6
[42] Haro-Poniatowski E, Jouanne M, Morhange J, Julien C, Diamant R, Fernández-Guasti M, Fuentes G and Alonso J 1998 Micro-raman characterization of WO_3 and MoO_3 thin films obtained by pulsed laser irradiation *Appl. Surf. Sci.* **127** 674–8
[43] Spevack P and McIntyre N 1992 Thermal reduction of molybdenum trioxide *J. Phys. Chem.* **96** 9029–35
[44] Tomás S, Arvizu M, Zelaya-Angel O and Rodríguez P 2009 Effect of znse doping on the photochromic and thermochromic properties of MoO_3 thin films *Thin Solid Films* **518** 1332–6
[45] Deb S 1968 Physical properties of a transition metal oxide: optical and photoelectric properties of single crystal and thin film molybdenum trioxide *Proc. R. Soc.* A **304** 211–31
[46] Dieterle M, Weinberg G and Mestl G 2002 Raman spectroscopy of molybdenum oxides part I. structural characterization of oxygen defects in MoO_{3-x} by dr UV/VIS, Raman spectroscopy and X-ray diffraction *Phys. Chem. Chem. Phys.* **4** 812–21
[47] de Castro Silva I, Reinaldo A C, Sigoli F A and Mazali I O 2020 Raman spectroscopy-in situ characterization of reversibly intercalated oxygen vacancies in α-MoO_3 *RSC Adv.* **10** 18512–8
[48] Fan X, Fang G, Qin P, Sun N, Liu N, Zheng Q, Cheng F, Yuan L and Zhao X 2011 Deposition temperature effect of RF magnetron sputtered molybdenum oxide films on the power conversion efficiency of bulk-heterojunction solar cells *J. Phys. D: Appl. Phys.* **44** 045101
[49] Diskus M, Nilsen O, Fjellvåg H, Diplas S, Beato P, Harvey C, van Schrojenstein Lantman E and Weckhuysen B M 2012 Combination of characterization techniques for atomic layer deposition MoO_3 coatings: from the amorphous to the orthorhombic α-MoO_3 crystalline phase *J. Vac. Sci. Technol.* A **30** 01A107
[50] Dang J, Zhang G-H and Chou K-C 2014 Phase transitions and morphology evolutions during hydrogen reduction of MoO_3 to MoO_2 *High Temp. Mater. Process.* **33** 305–12
[51] Lalik E 2011 Kinetic analysis of reduction of MoO_3 to MoO_2 *Catal. Today* **169** 85–92
[52] Wang L, Xue Z-L, Huang A and Wang F-F 2019 Mechanism and kinetic study of reducing MoO_3 to MoO_2 with CO-15 vol % CO_2 mixed gases *ACS Omega* **4** 20036–47